Construction and Building Materials 81 (2015) 140–153

Contents lists available at ScienceDirect

Construction and Building Materials

journal homepage: www.elsevier.com/locate/conbuildmat

Thermo-mechanical assessment of concrete microcracking damage due to early-age temperature rise

Franco Zunino [a], Javier Castro [b], Mauricio Lopez [c,d,*]

[a] Department of Construction Engineering and Management, School of Engineering, Pontificia Universidad Catolica de Chile, Vicuña Mackenna 4860, Casilla 306, Correo 22, Santiago, Chile
[b] Faculty of Engineering, Universidad del Desarrollo, Chile
[c] Department of Construction Engineering and Management, School of Engineering, Pontificia Universidad Catolica de Chile, Chile
[d] Center for Sustainable Urban Development (CEDEUS), Pontificia Universidad Catolica de Chile, Vicuña Mackenna 4860, Casilla 306, Correo 22, Santiago, Chile

HIGHLIGHTS

- Early-age time–temperature cycles damage observed on a variety of concrete mixtures.
- Mismatch between strain in concrete phases as main cause of cracking due to interfacial restraint gradients.
- Simplified two-phase micromechanical model proposed to assess thermal stresses.
- Detailed thermo-mechanical characterization of elastic modulus and CTE of phases.
- Interaction pressure (P) selected as indicator of thermal cracking damage level.

ARTICLE INFO

Article history:
Received 17 July 2014
Received in revised form 22 November 2014
Accepted 31 December 2014
Available online 2 March 2015

Keywords:
Temperature
Microcracking
Micromechanics
Degradation
Damage
Strain effect
Coefficient of thermal expansion
Mismatch
ITZ

ABSTRACT

The pursuit of high early-age strength concrete has led to mixtures with higher heat of hydration rates at early ages which produces higher temperatures and an overall increased risk of cracking. This study uses a two-phase micromechanical model to compute thermal stresses based on both coefficient of thermal expansion (CTE) and elastic Young's modulus (E) mismatches between aggregates and the cementitious matrix. Concrete specimens were prepared using four types of coarse aggregates (different CTE and E), and subjected to temperature cycles to generate thermal cracking. Fluorescence microscopy, compressive strength, dynamic elastic Young's modulus, and electrical resistivity were used to characterize the effect of this induced thermal cracking. Experimental results were in agreement with the two-phase model and it was concluded that the interaction pressure (P) between phases could be used to estimate the impact on the mechanical and transportation properties of a temperature gradient at early age.

1. Introduction

The main driving force in concrete construction over the last few decades has been construction speed, which has pushed the industry to develop high early-age strength concrete. These mixture designs promote the use of high cement contents, a low water-to-cement ratio (w/c), finer cements, and high-C_3A, contents, among others [1]. The resulting materials are commonly referred to as high-strength concretes [2]. Unfortunately, these mixtures are more prone to cracking [3] mainly because they tend to contain a higher paste fraction and exhibit more pronounced self-desiccation, chemical shrinkage [4], and autogenous shrinkage [2,5].

In addition, the higher cement content per unit volume and the use of finer cements increase both the initial rate and the total released heat of hydration, which can lead to an increase in temperature gradients inside the material. Differential thermal expansion of the concrete constituents may produce stresses and cracking that negatively affect the mechanical properties and durability of concrete [6–9]. These stresses occur in the early stages of

* Corresponding author at: Department of Construction Engineering and Management, School of Engineering, Pontificia Universidad Catolica de Chile, Chile. Tel.: +56 2 2 354 4245; fax: +56 2 2 354 4806.
E-mail addresses: fazunino@ing.puc.cl (F. Zunino), mlopez@ing.puc.cl (M. Lopez).

http://dx.doi.org/10.1016/j.conbuildmat.2014.12.126
0950-0618/

the concrete, when it is more vulnerable to cracking [5,10]. Furthermore, the increased temperature that accelerates cement hydration [11], produces lower quality and more porous calcium silicate hydrates (CSH) [12]. Moreover, concrete temperatures greater than 70 °C can induce chemical modifications of the hardened phases and lead to expansion due to delayed ettringite formation (DEF) [13–15].

The ACI committee 207 defines two types of thermal gradients that can lead to thermal stress development: a "*surface gradient*", which is the difference in temperature between two locations in the concrete element, and a "*mass gradient*", which is the difference in temperature between two periods of time, usually between the internal peak temperature and the annual average ambient temperature [16].

The surface gradient usually generates cracking due to differential expansion between the center and the edges of the structural elements due to differences in temperature at a certain instant [16,17]. The mass gradients usually generates cracking due to external restraint to thermal volume change, leading to thermal stresses [16].

A third kind of thermal cracking phenomena has its origin on the multi-phase nature of concrete and can be denoted as "*interfacial restraint gradient*". This interfacial restraint gradient originates in the thermo-mechanical mismatches between concrete constituents, i.e., aggregates and cementitious matrix [18–21], which lead to generation of internal restraint and thermal stresses. These stresses occur at early ages in the interfacial transition zone (ITZ), which exhibits lower strength and higher porosity compared with those of the bulk matrix [22–24].

Although several studies and efforts have been carried out in order to control and mitigate surface gradient [25–27] and mass gradient [28,29] effects, less information is available on interfacial restraint gradient effects. Moreover, a lack of knowledge of the effects of internal restraint and thermo-mechanical mismatches between concrete phases on key design parameters (i.e., compressive strength and elastic Young's modulus), leads to uncertainty in the actual load-bearing capacity of concrete subjected to high temperatures at early age. Few studies exist in the assessment of permeability of damaged concrete [30–32], which further affects durability, but still not directly related to thermal cracking by interfacial restraint gradient. Understanding how the aggregate and cementitious matrix properties affect the thermo-mechanical mismatches is crucial in assessment and design of concrete mixtures with reduced microcracking risk for the purpose of ensuring mechanical and durability performance.

2. Objective

The aim of this research is assess the impact of aggregate and matrix thermo-mechanical properties (CTE and elastic Young's modulus) mismatches on thermal stresses and potential cracking of concrete by using a micromechanical model.

3. Proposed two-phase micromechanical model

It is widely accepted that concrete is most accurately represented as a three-phase material [23], including the aggregates, cement paste, and the ITZ between them. The ITZ has been described as the explanation for the quasi-ductile behavior of concrete [24], and several studies attempted to characterize and understand this particular phase [33–36]. Despite the recognized relevance of the ITZ in explaining concrete behavior, the inherent difficulties in measuring the mechanical and thermal properties at a micro-scale makes it impractical to fully incorporate the ITZ in models. Advances have been made in this matter using nano-indentation, which consistently shows that the ITZ has higher porosity and lower modulus of elasticity than the bulk matrix. However, most of these studies also verify the high variability of elastic properties of the ITZ, turning the selection of a specific value for modeling less representative and highly inaccurate [33–35,37,38]. For this reason, a widely adopted approach considers concrete as a two-phase material: the coarse aggregates and the bulk matrix of mortar surrounding them. This simplification has been successfully used to model and predict relevant properties of concrete, i.e., elastic Young's modulus and coefficient of thermal expansion [21,39–41].

Another assumption of the model is that the cementitious matrix exhibits an elastic behavior. In reality, creep and stress relaxation are relevant phenomena occurring early ages [1,42–44], that are not represented in the model. Since the inelastic behavior decrease stresses [1] at the ITZ, the stresses computed with the model are higher than the exact thermal stresses, giving a conservative approach.

Due to the composite nature of concrete, understanding the elastic and thermal compatibility of its components is crucial for predicting and modeling concrete behavior with reasonable accuracy [19]. In particular, temperature fluctuations in concrete during cement hydration produce differential strains between the concrete phases and thus the thermally induced stresses that generate microcracking [19,45]. Assuming a uniform temperature distribution in all concrete phases, the main thermo-mechanical variables that control the magnitude of these stresses are the differences in elastic Young's modulus (E) and the coefficient of thermal expansion (CTE) of the aggregates and the matrix [20,21]. The occurrence of differential strains is well explained by the mismatch between the thermo-mechanical parameters of the aggregates and the matrix.

Based on the general formulation presented by Zhou et al. [21], a two-phase model is proposed in this work to assess the thermal stresses between concrete composites in different thermo-mechanical mismatch scenarios. As shown in Fig. 1, the micromechanical model consists of a spherical aggregate particle of radius a surrounded by an infinite thickness spherical shell matrix. This model applies a temperature change from T_0 to T_1, which will be denoted as ΔT. This parameter represents the temperature variation of a particular place at two different time periods.

Properties and values related to the aggregate and matrix phase will be denoted with the subscripts 1 and 2, respectively. The radial strain (ε_r) and the tangential strain (ε_t) generated in the interface between the aggregate and the bulk matrix are given by [46]:

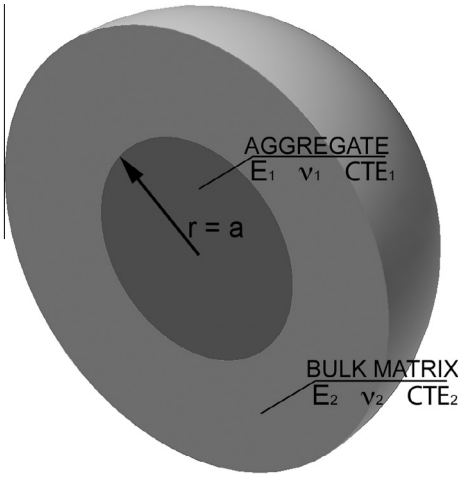

Fig. 1. Two-phase model of concrete consisting of an aggregate particle surrounded by an infinite mortar matrix.

$$\varepsilon_{ri} = \frac{1}{E_i}(\sigma_{ri} - 2\nu_i\sigma_{ti}) + \alpha_i\Delta T \quad (1)$$

$$\varepsilon_{ti} = \frac{1}{E_i}((1-\nu_i)\sigma_{ti} - \nu_i\sigma_{ri}) + \alpha_i\Delta T \quad (2)$$

where the subscript i refers to the considered phase (1 or 2), σ_r and σ_t are the radial and tangential stress, respectively, and ν_i is the Poisson ratio of phase i. It can be assumed that the differential thermal deformations of the concrete phases are represented by an equivalent thermal interaction pressure (P) present in the interface between them (Fig. 2a and b). It should be noted that in a 2D formulation at the equator of the spherical aggregate the external shell is equivalent to a cylindrical section. As derived from a simple spherical model of internal radius a and infinite wall thickness with interaction pressure P applied on its cavity (Fig. 2b) at a distance r from the center, the stresses are represented as described in [20]:

$$\sigma_{r2} = -2\sigma_{t2} = -P\frac{a^3}{r^3} \quad (3)$$

In this convention, positive values represent tensile stresses. Similarly, for a solid sphere of radius a subjected to an external pressure P (Fig. 2a), the radial and tangential stresses are given by:

$$\sigma_{r1} = \sigma_{t1} = -P \quad (4)$$

Substituting Eqs. (3) and (4) into Eqs. (1) and (2) and applying the strain compatibility conditions at $r = a$ ($\varepsilon_{t1} = \varepsilon_{t2}|_{r=a}$), the value of the thermal interaction pressure P is obtained as:

$$P = \frac{\Delta T(\mathrm{CTE}_1 - \mathrm{CTE}_2)}{\frac{1+\nu_2}{2E_2} + \frac{1-2\nu_1}{E_1}} \quad (5)$$

The radial and tangential stress and strain for both phases can be obtained by substituting the obtained value of P into Eqs. (1) through (4).

As expected, Eq. (5) clarifies the linear relationship of P with the CTE mismatch between the aggregate and the matrix represented by the coefficient ($\mathrm{CTE}_1 - \mathrm{CTE}_2$), and the non-linear relationship of P with the elastic mismatch between the aggregate and the matrix represented by E_1 and E_2. From analysis of Eqs. (3) through (5), it can be observed that with a positive value of ΔT (temperature increment), if $\mathrm{CTE}_1 > \mathrm{CTE}_2$, tensile stresses are generated in the tangential direction of the second phase (matrix), and thus microcracks are more likely to be generated in the radial direction from the aggregate particle (Fig. 3a). Similarly, if $\mathrm{CTE}_1 < \mathrm{CTE}_2$, the tensile stresses are oriented in the radial direction in both phases, and microcracks are prone to appear with a tangential orientation between the phases surrounding the aggregate particle (Fig. 3b).

The interaction between fine aggregate particles and cement paste is neglected in the proposed model because ITZ and therefore

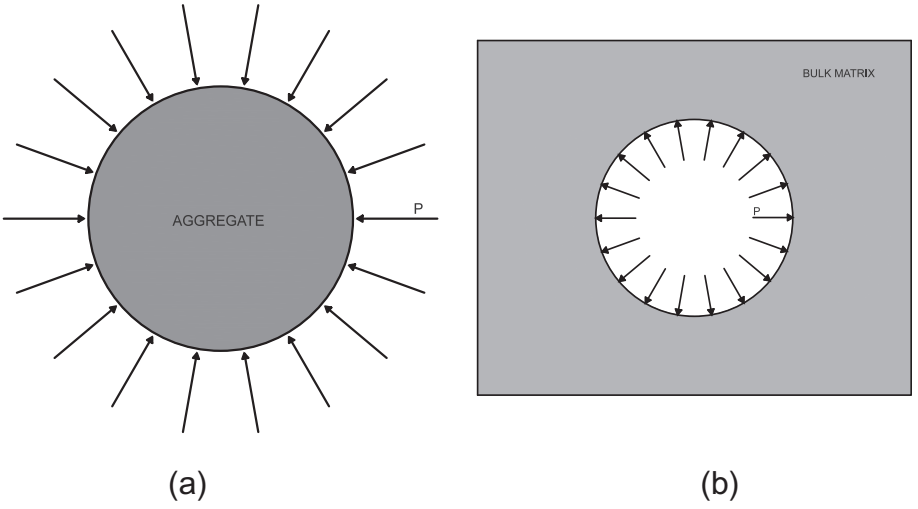

Fig. 2. (a) Solid sphere of radius a with applied external pressure P applied; (b) spherical shell of infinite thickness with internal pressure P.

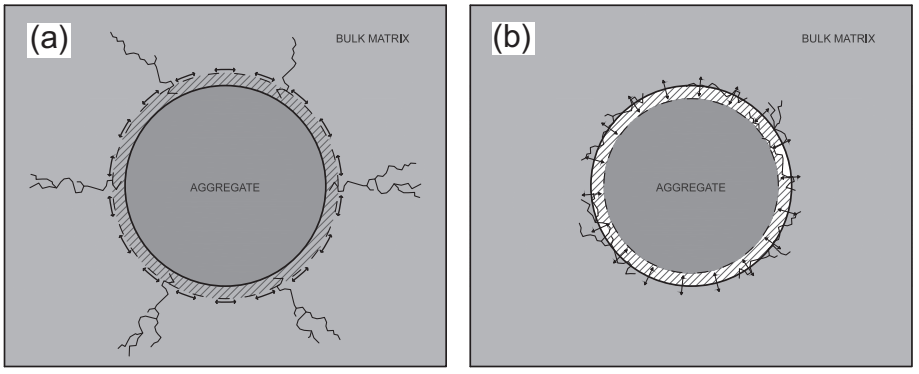

Fig. 3. (a) Tangential tensile stresses and radial microcracks induced when $\mathrm{CTE}_1 > \mathrm{CTE}_2$ and $\Delta T > 0$; (b) radial tensile stresses and tangential microcracks induced when $\mathrm{CTE}_1 < \mathrm{CTE}_2$ and $\Delta T > 0$.

microcracking are most likely to occur around large aggregate particles [23] if both, large and fine particles, have similar angularities and surface texture [47].

4. Thermal history and cement hydration

An increase in temperature of concrete, especially at early ages, significantly affect the strength development due to the faster cement hydration [1]. For this reason, many researchers have focused their efforts on developing relationships between temperature and strength [48]. In addition, the hydration products generated at accelerated rates due to higher temperatures exhibit a coarser and more porous structure [12], which explains the lower long-term strength reached by concrete cured at higher temperatures [42,49] compare with those cured at 20 °C.

Saul [50] introduced the maturity concept 60 years ago to account for this effect. According to his research, maturity is the product of temperature history ($T(t)$) and time (Eq. (6)), accounting for a datum temperature (T_D) below which hydration is unlikely to occur [51,52]:

$$M = \int_0^t (T(t) - T_D)dt \tag{6}$$

The ASTM C1074 [53] recommends use of a datum temperature of 0 °C for Type I Portland cement cured between 0 °C and 40 °C. An alternative approach to the maturity function is the equivalent age concept (t_{eq}), defined as the curing time required at a reference temperature (T_R) to achieve the same maturity level as a concrete that undergoes the actual time–temperature cycle [49,52,54]. The most widely used function for computing equivalent age at a reference temperature T_R is based on the Arrhenius equation [53,55]:

$$t_{eq}(T_R) = \sum_{t=0}^{t} e^{\frac{E_a}{R}\left(\frac{1}{T_C} - \frac{1}{T_R}\right)} \times \Delta t \tag{7}$$

where $t_{eq}(T_R)$ is the equivalent age at the reference temperature T_R (K), T_C (K), is the concrete temperature, Δt is the time interval (days or hours), R is the ideal gas constant (8.314 J/mol/K), and E_a is the apparent activation energy (in J/mol), which combines the temperature sensitivity of the several chemical reactions occurring during cement hydration into one parameter [55]. The same study presents a method used to determine E_a using isothermal calorimetry, which provides a useful tool for accurately modeling the cement hydration kinetics and computing equivalent ages at which samples subjected to different time–temperature cycles can be assumed to have the same degree of hydration.

5. Experimental program

The variety of aggregates used in concrete mixtures poses inherent challenges to characterization and engineering of key properties required to improve performance and mechanical behavior in a cementitious matrix [18]. Each type of aggregate type contains a mineralogical composition that conditions the fundamental thermo-mechanical parameters E_1 and CTE_1, of that particular rock. This fact makes an individual assessment of the CTE and elastic mismatch between the aggregate and the bulk matrix phase impossible because both variables necessarily vary together when the aggregate mineralogy changes.

Temperature variations generate aggregate thermal strain that can be simply denoted as $CTE_1\Delta T$, where CTE_1 is the aggregate CTE. A variation in α_1 changes the thermal stress, increasing or decreasing the CTE mismatch ($CTE_1 - CTE_2$) with the matrix. In parallel, a variation in the aggregate elastic Young's modulus E_1 has an non-linear impact on the magnitude of the thermal stress induced by the strains generated due to a temperature change, as shown in Eq. (5). Because E_1 and CTE_1 are given for a certain aggregate and cannot be varied independently, different time–temperature cycles were used to artificially hold the aggregate thermal strain constant ($CTE_1\Delta T$). Thus, the same aggregate expansion scenario can be achieved over a wide range of E_1 values.

Similarly, for a given aggregate, time–temperature cycle adjustments can be used to simulate aggregate thermal strain variations while holding E_1 constant. This goal is achieved by modification of the ΔT term in the $CTE_1\Delta T$ expression. The effects of this external handling on the stresses generated between the concrete phases are equivalent to an apparent CTE_1 modification for a given aggregate of known elastic Young's modulus E_1.

The values of υ_1 and υ_2 were assumed as 0.2 [21]. Because the value of P represents a uniform stress in the aggregate and bulk matrix surfaces, the effect of this assumption has low relevance compared with the elastic Young's modulus and CTE mismatches. A representation of the thermo-mechanical experimental design is shown in Fig. 4, and details of the considered aggregates will be presented in the Materials and Methods section.

5.1. Design of time–temperature cycles

Four different types of coarse aggregates were selected to explore a wide range of thermo-mechanical properties: expanded shale (LA, lightweight aggregate), calcareous gravel (CA, normal weight aggregate), siliceous gravel (SA, normal weight aggregate), and magnetite (HA, heavyweight aggregate).

Four experimental points were defined in the iso-thermal strain axis, one for each type of aggregate used. Temperature adjustments were chosen accordingly to account for the different CTE_1 value of each aggregate while holding $CTE_1\Delta T$ constant in all cases (determination of aggregate properties will be presented in next section). To explore the effects of the apparent CTE_1 variation (iso-stiffness axis), the LA and SA were selected due to their significantly different stiffnesses as well as the broad use and availability in the SA case. The experimental points are presented schematically in Fig. 4.

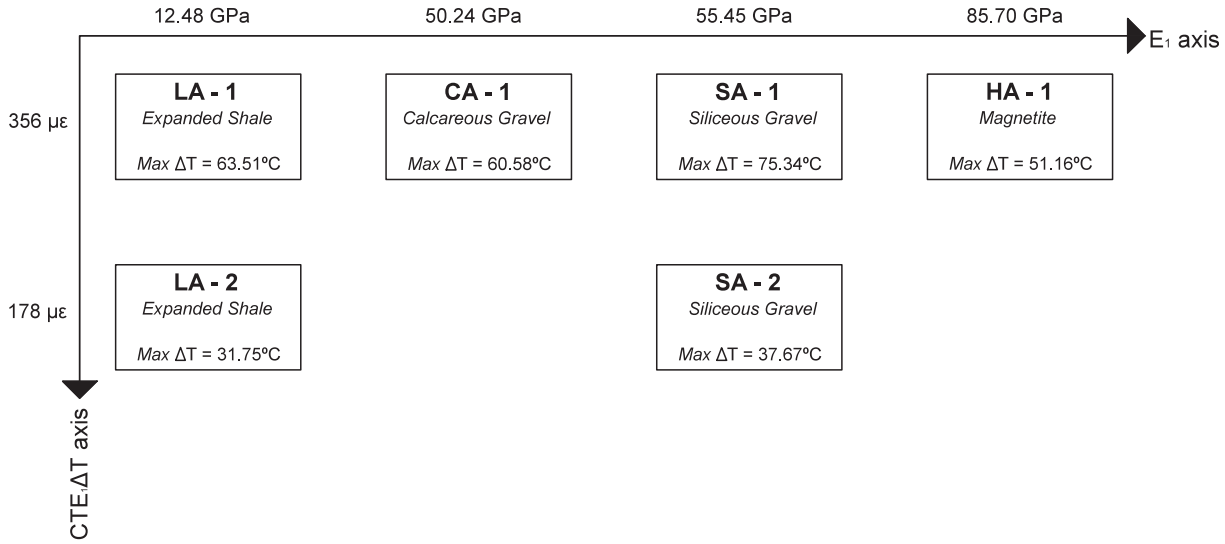

Fig. 4. Experimental points explored over a conceptual two-axis thermo-mechanical design.

The time–temperature cycles were based on a real temperature record obtained from a massive concrete foundation. The cooling portion was adjusted to exhibit symmetry with the starting heating ramp, and the general shape of the thermal cycle is shown in Fig. 5. The values of T_1, and T_{MAX} (1-day and maximum temperature, respectively) and the aggregate maximum thermal strains are presented in Table 1 for each of the experimental points. Max ΔT was computed as the difference between T_{MAX} and T_0 (20 °C).

5.2. Concrete mixture proportions

The concrete mixtures were produced using four different types of coarse aggregates. The same base mortar matrix was used for all mixtures and was based on siliceous fine aggregate and Type I ordinary Portland cement (OPC). In all cases, the coarse aggregate volume fraction was 37.5%, and a water to cement ratio of 0.55 was selected based on the literature to minimize the effects of autogenous shrinkage [5,56–59], so thermal strain is the main phenomenon inducing stresses [60]. OPC and fine aggregate dosage was fixed at 350 kg/m^3 and 820 kg/m^3, respectively.

Fifteen 10 × 20 cm cylinders, six 10 × 10 × 30 cm prism specimens, and eight 2.5 × 5.0 cm cylinders were cast for each of the six experimental points studied (Fig. 4). The specimens were placed at an environmental chamber for 24 h at (20 ± 3) °C and covered with plastic sheet to avoid evaporation until removed from the molds.

5.3. Thermal damage testing

After removal from the molds, the specimens were weighed and randomly assigned to the thermal cycle (TC) and equivalent age curing (TE) groups. Five10 × 20 cm cylinders, three 10 × 10 × 30 cm prisms, and four 2.5 × 5.0 cm cylinders each composed the TC and TE specimen groups.

The TC group refers to specimens subjected to the time–temperature cycles described in Table 1 and were intended to measure the effect of thermal stresses on the concrete properties. The TE group consisted of a set of specimens identical to the TC group and intended to serve as a non-damaged material reference; the specimens in this group were cured at (20 ± 3) °C for the equivalent age calculated using Eq. (7), and the time–temperature cycle of the TC group. The initial tests on instrumented specimens showed that the maximum temperature gradients between the core and surface (surface gradient) was only 1.5 °C regardless of the specimen size and shape, which was sufficient to neglect the surface gradient effect and to consider damage produced by a pure interfacial restraint gradient effect [42]. Specimens from the TC and TE groups were sealed using aluminum tape before undergoing thermal cycles and curing at 20 °C, respectively. This method proved to be effective in avoiding water losses at high temperatures, which was relevant to avoid the concrete swelling and drying/shrinkage effects present in other curing methods.

For modeling purposes, the reference frame at which stress and strain are assumed to be zero occurs at the beginning of each thermal cycle. Thus, all the computed stresses are attributed to the time–temperature cycles imposed to the samples.

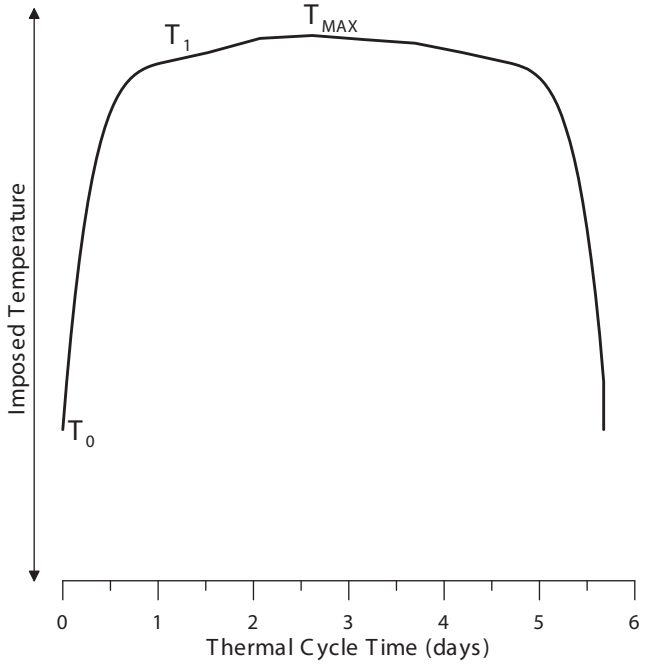

Fig. 5. Basic shape of the time–temperature cycle applied to the concrete specimens.

Table 1
Temperature parameters for each experimental point.

Experimental point	T_1 (°C)	T_{MAX} (°C)	Max ΔT (°C)	Max $\alpha_1 \Delta T$ ($\mu\varepsilon$)
LA-1	79.4	83.5	63.5	356
CA-1	76.7	80.6	60.6	356
SA-1	90.5	95.3	75.3	356
HA-1	67.9	71.2	51.2	356
LA-2	49.7	51.8	31.8	178
SA-2	55.3	57.7	37.7	178

5.3.1. Fluorescence microscopy

Fluorescence optical microscopy has been proven as a powerful technique for performing qualitative and quantitative measurements of microcracking in concrete [61–64]. In this study, fluorescence microscopy was used as a tool for qualitative identification of the crack density and morphology in specimens subjected to the time–temperature cycle and the equivalent-age curing. Samples of 1 cm in height were cut from the 2.5 × 5.0 cm cylinder specimens of the TC and TE groups using a low-speed saw. The samples were cleaned in an ultrasonic bath for 10 min using iso-propanol as cleaning medium. After removal from the bath, the samples were cleaned with compressed air, dried at 35 °C and 720-mmHg vacuum, and stored under those conditions for 2 h. The samples were finally impregnated using an ultra-low viscosity and high-hardness resin combined with fluorescein (FITC) as a fluorochrome. To avoid additional exposure of the samples to temperatures that could result in unintended microcracking, the resin was cured using UV radiation for 48 h at a laboratory temperature of 20 °C. After curing, the samples were polished using a standard grinding machine prior to observation. The TE samples were prepared using the same procedure as the TC samples and were intended to provide a reference for cracking generated by the preparation method and other phenomena unrelated to the thermal cycle.

5.3.2. Compressive strength

The compressive strength was measured on 10 × 20 cm cylinder specimens of each TC and TE group. For the TC and TE specimens, tests were performed after the thermal cycle and equivalent age curing periods, respectively. After completion of electrical resistivity testing, the specimens were also tested for compressive strength. It should be noted that no significant difference in results were observed between the saturated and non-saturated specimens.

5.3.3. Dynamic elastic Young's modulus

The dynamic elastic Young's modulus was measured on 10 × 10 × 30 cm prism specimens of the TC and TE groups according to the ASTM C215 procedure [65]. This method was selected due to its suitability and sensitivity to measurement of concrete damage due to microcracking in freeze-thaw tests. It should be mentioned that the dynamic elastic Young's modulus test is based on measurement of the fundamental resonant frequencies of the specimen and is therefore non-destructive.

5.3.4. Electrical resistivity

The electrical resistivity was measured in 10 × 20 cm cylinder specimens of the TC and TE groups based on the axial-measurement method described by Spragg et al. [66] to compare changes in the concrete pore percolation due to the presence of microcracks. In this method, two stainless steel plates are placed at the ends of the 10 × 20 cm cylinder and connected to the same surface resistivity meter used in the Wenner probe apparatus [67]. The obtained electrical resistance values are normalized by the cross-sectional area-to-length ratio of the cylinder to calculate the bulk resistivity of the specimen. Three cylinder specimens were randomly selected, the aluminum tape was removed, and the specimens were submerged in water for 24 h at 20 °C to achieve saturation of cracks before testing.

6. Materials characterization

6.1. Cementitious matrix constituents

To accurately predict the cement hydration using the Arrhenius equation and calculate the equivalent age (Eq. (7)), an accurate measure of the activation energy (E_a) is required. The procedure based on isothermal calorimetry described by Poole et al. [55] was used. While other methods to determine E_a are available such as the compressive strength method proposed in ASTM C1074 for strength estimating purposes [53,68], isothermal calorimetry mea-

sures directly heat evolution and thus, this method would seem to be a better approach to degree of hydration estimation than compressive strength [69]. The OPC phase composition was determined using X-ray diffraction (XRD) and Rietveld refinement analysis. Fluorite was used as an internal standard to account for the amorphous fraction and to correct the Rietveld results based on the procedure proposed by Chancey et al. [70]. The identified main phases and the phase composition are shown in Table 2.

Isothermal calorimetry tests were carried out using TAM Air isothermal calorimeter at 10 °C, 20 °C, 32 °C and 40 °C. In all cases, a 0.55 w/c cement paste was used. The maximum heat of hydration (H_u) used to normalize the heat curves and obtain the degree of hydration plots was calculated using the equation proposed by Bogue [71]:

$$H_u = 500 \cdot p_{C_3S} + 260 \cdot p_{C_2S} + 866 \cdot p_{C_3A} + 420 \cdot p_{C_4AF} + 624 \cdot p_{SO_3} + 1186 \cdot p_{FreeCa} + 850 \cdot p_{MgO} \quad (8)$$

where p_x represents the mass ratio of phase x to the total cement material. A commercial non-linear regression package was employed to adjust the model presented in [55] with the obtained degree-of-hydration plots. The computed value for H_u was 460.17 J/g, which is in good agreement with total heat of hydration values reported for numerous other OPC samples [55,71]. The apparent activation energy was subsequently calculated using the equation proposed by Schindler [11], and the resulting value was 45,880 J/mol. This parameter was used to compute the equivalent ages using Eq. (7) for all experimental points. The heat plots together with the regression fit at each temperature and the Arrhenius plot of the applied OPC are presented in Fig. 6.

The bulk matrix CTE (CTE_2) was measured over time using 2.54 × 2.54 × 25.4 cm prismatic specimens and a digital length comparator. The applied mixture proportions were the same as those used for concrete but without the coarse aggregate. Because the matrix CTE is influenced by the relative humidity (RH) content [72], the specimens were sealed using aluminum tape after removal from the molds to avoid desiccation during the testing procedure. Samples were then tested and stored in this sealed unsaturated condition. Fifteen specimens were prepared, and three of each type were tested daily from 2 d to 28 d in age and every week up to 66 d. The specimens were heated to 50 °C, measured in the length comparator (L_{50}), and subsequently cooled to room temperature (T_{LAB}) for a new length measurement (L_{LAB}). The temperature was recorded using a thermocouple embedded within one specimen subjected to the same time–temperature cycle and used exclusively for temperature recording. The CTE of the matrix (CTE_2) was computed using Eq. (9):

$$CTE_2 = \frac{\frac{L_{50}-L_{LAB}}{L_{LAB}}}{50 - T_{LAB}} \quad (9)$$

Table 2
QXRD analysis of the OPC using the Rietveld refinement and fluorite as an internal standard.

Mineral name	Formula	Rietveld presence (% by wt.)
Quartz	SiO_2	1.0
Bassanite	$2CaSO_4(H_2O)$	3.1
Anhydrite	$CaSO_4$	1.1
Calcite	$CaCO_3$	1.8
Fluorite (I.S.)	CaF_2	11.5
Lime	$CaCO_3$	0.7
C_3A cubic	$3CaO{\cdot}Al_2O_3$	8.6
Alpha C_2S	$2CaO{\cdot}SiO_2$	5.3
Beta C_2S	$2CaO{\cdot}SiO_2$	1.7
Ferrite (C_4AF)	$4CaO{\cdot}Al_2O_3{\cdot}Fe_2O_3$	6.8
Alite (C_3S)	$3CaO{\cdot}SiO_2$	58.4
		I.S. = internal standard

The results for CTE tests of the bulk matrix are presented in Fig. 7 in which a clear increasing trend is observed during the first 20 d. This observation is consistent with previous results [72] and is attributed to the reduction in autogenous RH. Even considering this RH reduction, the selected w/c ratio of 0.55 has shown to be high to maintain RH above critical values [73,74], and to neglect effects of autogenous shrinkage. After 40 d of curing, the CTE change with time stabilizes, presumably due to a reduction in the hydration rate.

6.2. CTE and E of coarse aggregates

The aggregate CTE (CTE_1) was measured using thermo-mechanical analysis (TMA) using a TA 943 instrument. Tests were carried out between −20 °C and 120 °C in samples with four different grains for each type of aggregate. For the LA aggregate, eight grains were considered in four tests parallel to the cleavage plane and four tests perpendicular to the cleavage plane. The grains were cooled from room temperature (approximately 25 °C) to −30 °C and held until the temperature stabilized. All aggregates were test-

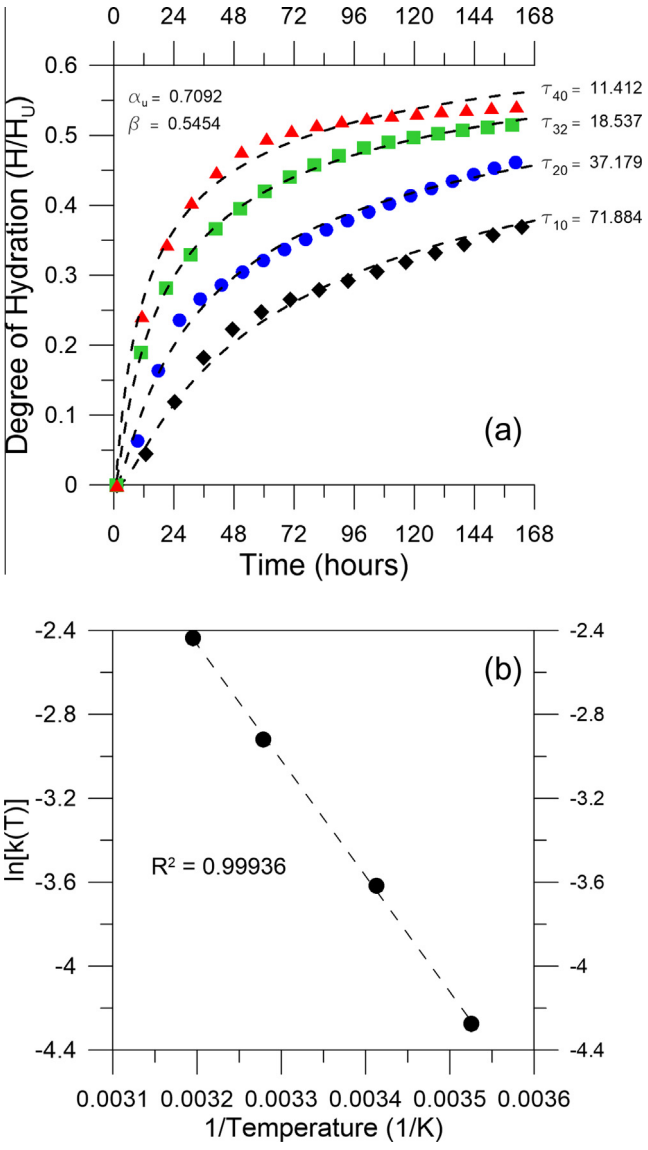

Fig. 6. (a) Isothermal calorimetry results (dots) and exponential regression (dashed line); (b) arrhenius plot of OPC.

ed in oven dry condition. The specimen was heated to 130 °C at a rate of 5 °C/min. The test was performed under a load of 1 g (10 mN) and a flow of dry nitrogen at 25 mL/min. If the data showed excessive noise, extreme discontinuities, or outlier behavior due to sample placement or outer vibration, the data collection process was halted, the grain was re-cooled, and the test was restarted. In all cases, good linearly between thermal deformation and temperature increase was observed in the range explored. The averages and standard deviations of the measured CTE values are summarized in Table 3.

The aggregate elastic Young's modulus (E_1) of the aggregate grains is difficult to measure due to the irregular shapes that they present. Several composite models were proposed for estimating the concrete elastic Young's modulus based on matrix and aggregate properties [40]. The Hirsch model was selected due to good agreement between the predicted and theoretical values [39]. In this study, the concrete and bulk matrix elastic moduli (E_C and E_m, respectively) were measured to compute the aggregate elastic Young's modulus using Eq. (10) with knowledge of the volume fraction of the aggregate (V_a). The concrete mixtures were assembled following the procedure proposed by Moreno et al. [75] using a V_a equal to 0.4. The x parameter was experimentally adjusted using steel and aluminum chunks as coarse aggregates and was estimated at 0.5. Values for each aggregate type are presented in Table 3:

$$E_C = \frac{1}{x\left[\frac{V_a}{E_1} + \frac{1-V_a}{E_m}\right] + (1-x)\left[\frac{1}{V_a E_1 + (1-V_a)E_m}\right]} \tag{10}$$

7. Results and discussion

7.1. Fluorescence microscopy

Thermo-mechanical characterization of the coarse aggregates (Table 3) and the bulk matrix (Fig. 7) showed that all four aggregates had a CTE significantly lower than that of the matrix (i.e., $CTE_1 < CTE_2$), and this difference increases with the age of the matrix. Based on the proposed two-phase micromechanical model, these results suggest that upon heating, the expected microcracks are more likely to be oriented similar to those in Fig. 3b because the tensile stresses will develop in the radial direction. This presumption was confirmed based on fluorescence microscope observation of TC specimens of all experimental points considered. The microcracks were distributed primarily along the ITZ surrounding the aggregates, as shown in the micrographs (Fig. 8a–f) for all aggregate types and time–temperature cycles imposed. Dark field (DF) images of the same micrograph for each fluorescence picture are included to aid in phase identification.

To assure that the microcracks observed in Fig. 8 were in fact due to thermal stresses and not due to drying shrinkage or artifacts that occurred during sample preparation, careful observations of TE samples were conducted. The presence of microcracks was significantly lower compared with that of the TC samples, as shown in Fig. 9.

Table 3
Aggregate CTE (CTE_1) and elastic Young's modulus (E_1) computed using the compound Hirsch model.

Aggregate type	Specific gravity (SSD) ρ_a	Average CTE_1 (10^{-6}/°C)	STD (10^{-6}/°C)	Average E_1 (GPa)	STD (GPa)
LA	1.628	5.61	0.52	12.48	0.45
CA	2.566	5.88	2.73	50.24	8.37
SA	2.698	4.73	0.74	55.45	2.80
HA	4.220	6.96	0.52	85.70	2.40

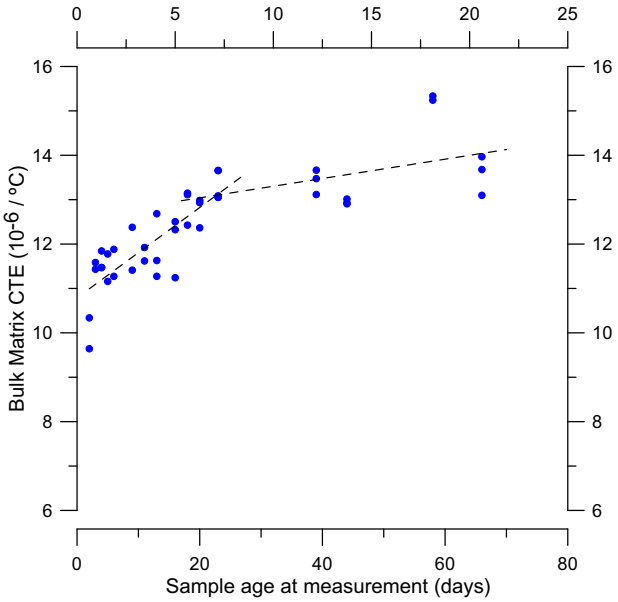

Fig. 7. Bulk matrix CTE (CTE_2) measured over time.

Fluorescence microscopy observations confirmed the presence of microcracks at different levels and extensions in the TC samples. The presence of incremental damage due to time–temperature cycles validates the need for statistical analysis of the influence of such damage on the mechanical and transport properties (compressive strength, elastic Young's modulus, and electrical resistivity) and the use of mechanical parameters in the two-phase micromechanical model.

In addition to the thermal stresses and damage, it should be noted that a lower quality and higher porosity CSH matrix would have been generated due to the increased rate of reaction in the TC samples. Thus, the overall damage to the concrete is due to the increased thermal stresses and increased matrix porosity.

7.2. Compressive strength

The results of the compressive strength tests are shown in Fig. 10 and are divided into two charts (a and b) according to the experimental program design: the first one shows the iso-thermal strain and the second one displays the iso-stiffness experimental points, as defined on Section 5.1. The hatched bars show the TE results, and the overlapped grey bars present the TC results. The gap between the gray and the green-dashed bars represents the strength loss due to thermally induced microcracks.

Statistically significant strength losses were observed in all of the high aggregate expansion series (Fig. 10a). A greater relative strength loss was observed in the SA-1 specimens attributed to the high CTE mismatch combined with a relatively high elastic Young's modulus of this aggregate, which leads to an increased deformation of the matrix and a high maximum interaction pressure (P) value. It is interesting to note that a high stiffness aggregate such as the HA will not necessarily lead to high thermal stresses between the aggregate and the bulk matrix because the value of P is determined not only by the elastic Young's modulus of the aggregate but also by its CTE. Particularly in the HA case, its high elastic Young's modulus is compensated to a certain extent with the reduced CTE mismatch between the HA and the bulk matrix. This situation yields a lower value of P compared with that of the SA and CA. In the same way, although the LA has a higher CTE mismatch compared with HA, its stiffness is significantly low-

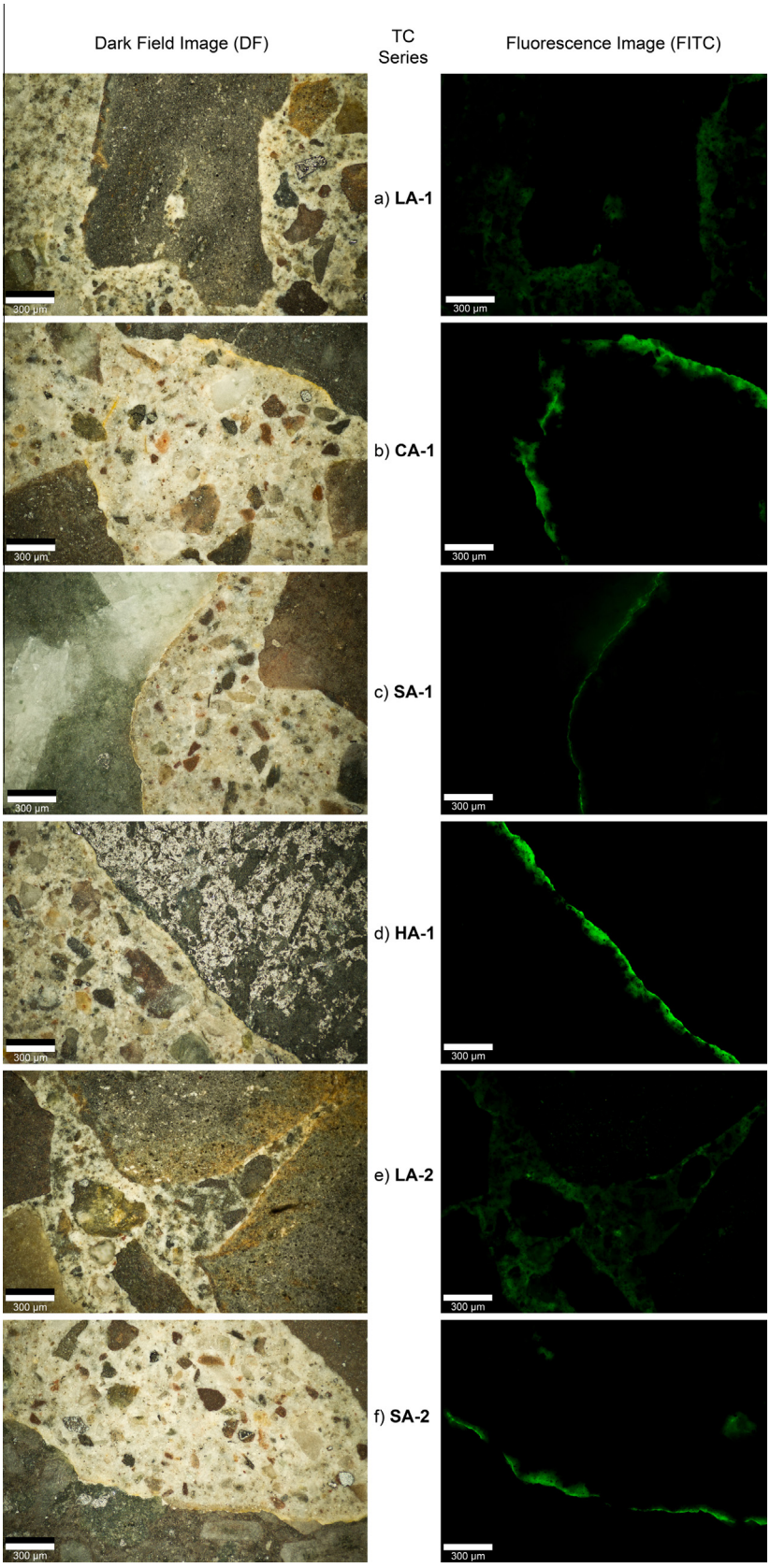

Fig. 8. Dark field (DF) and fluorescence images of microcracks observed on the ITZ on all experimental series (a–f).

er, resulting in the lowest computed maximum *P* value. All of these theoretical derivations based on aggregate and bulk matrix characterizations are observed in the compressive strength results.

Fig. 10b shows that no significant strength losses were observed in the LA-2 specimens, which imply that the thermal stresses generated were lower than the developing tensile strength of the

matrix, and thus, significant microcracking did not occur during the thermal cycle.

To correlate the experimental results with the theoretical derivations from the micromechanical model, two reference parameters were selected. The interaction pressure P, due to the direct relationship between this value and the stresses in both phases and its ease of computation, making it suitable to be used as a practical index of thermal damage. In addition, the radial deformation of the bulk matrix ε_{r2} was selected because tensile stresses will occur primarily in this direction according to the model (Fig. 3b).

The average compressive strength performance ratios were computed by dividing the average strength of the TC specimens into the corresponding average strength of the TE specimens for each of the six experimental points. These ratios are a numerical representation of the strength losses for which a ratio of 1 implies no loss in compressive strength of TC specimens compared with that of the TE specimens. The plots of TC/TE compressive strength ratios against their corresponding maximum P (Fig. 11a) or ε_{r2} (Fig. 11b) values achieved during the time–temperature cycles were analyzed, and a non-linear trend was observed.

It is interesting to note that the computed ε_{r2} values are consistent with the strains that cement paste and concrete are able to withstand before rupture. In the case of SA-1, which presented the most pronounced loss in strength, the maximum radial matrix strains were close to 0.003 mm/mm, suggesting that the maximum strain capacity on average of the matrix was overcome. The non-

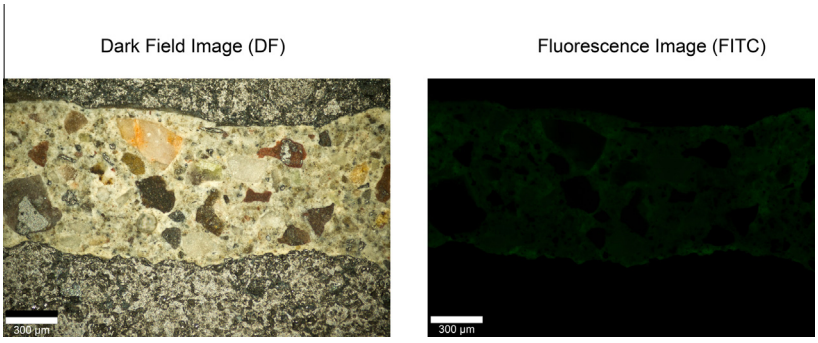

Fig. 9. Dark field (DF) and fluorescence images of the ITZ zone in samples not subjected to thermal stresses.

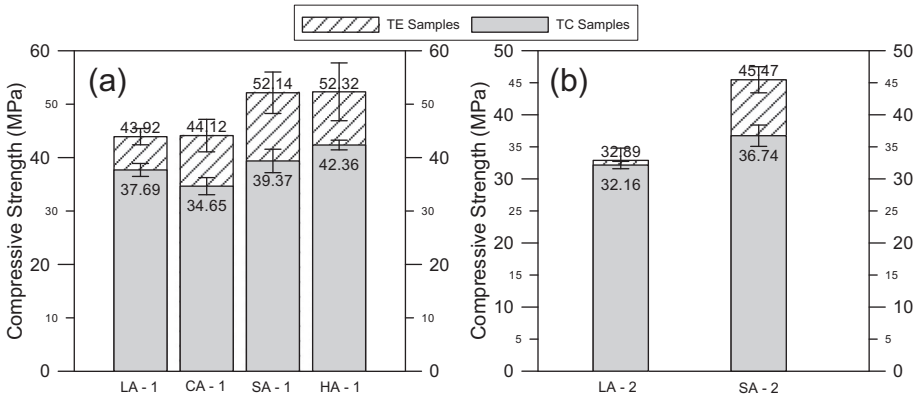

Fig. 10. Compressive strength results of TC and TE specimens: (a) high aggregate thermal expansion level; (b) low aggregate thermal expansion level. Error bars represent the standard deviation of the average of three samples.

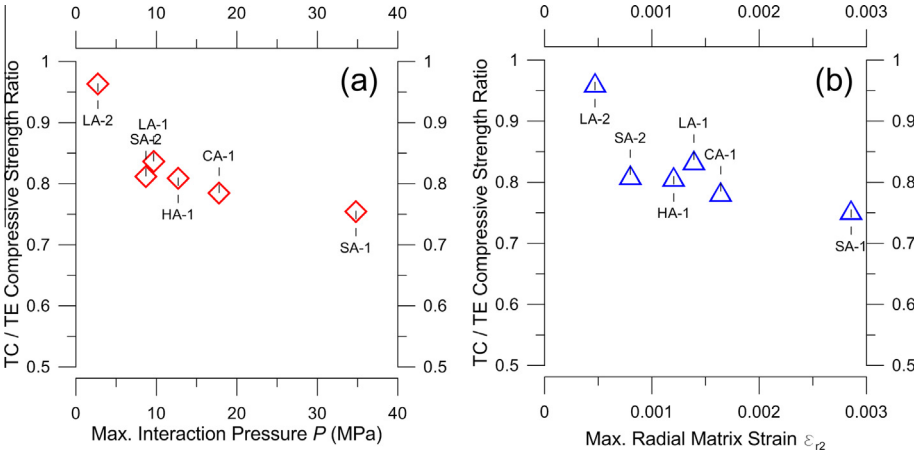

Fig. 11. (a) TC/TE compressive strength ratios correlated with P values; (b) TC/TE compressive strength ratios correlated with ε_{r2} values.

linear behavior of the compressive strength loss trend could be attributed to presence of the ITZ, neglected in the proposed model. The quasi-brittle behavior of concrete under compression is attributed to multiple microcrack development on the ITZ [24]. In addition, formation of microcracks is not uniform over the loading range [76]. Thus, the relationship between P and compressive strength is expected to be non-linear.

7.3. Dynamic elastic Young's modulus

The results of measurements of the dynamic elastic Young's modulus are presented in Fig. 12 using the same data distribution described for compressive strength.

Consistent with the findings for compressive strength, larger elastic Young's modulus losses for the TC concrete specimens were observed in SA-1 and CA-1. Statistically significant differences between the corresponding TC and TE results were observed in all of the high aggregate expansion series (Fig. 12a) and only in the SA-2 specimens in the low aggregate expansion level (Fig. 12b).

Similar to the compressive strength results, the average elastic Young's modulus performance ratios were computed by dividing the average elastic Young's modulus of TC specimens into the corresponding average result of the TE specimens for each of the six experimental points. Plots of the TC/TE elastic Young's modulus ratios against their corresponding maximum P (Fig. 13a) and ε_{r2} (Fig. 13b) values achieved during the thermal cycle were studied.

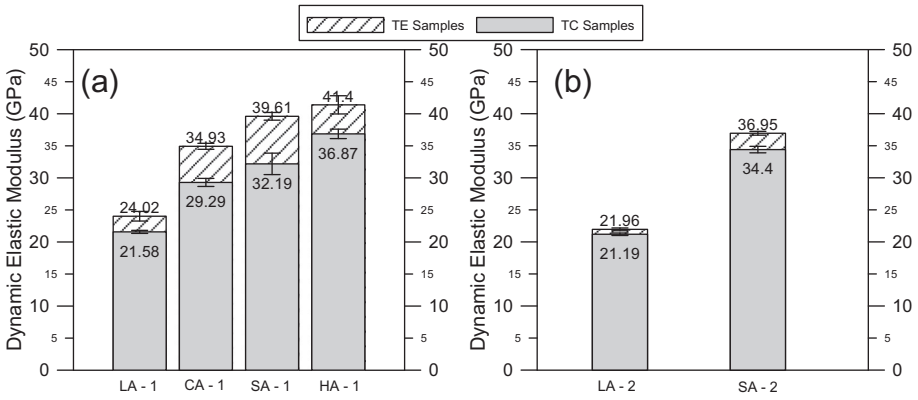

Fig. 12. Dynamic elastic Young's modulus results of TC and TE specimens: (a) high aggregate thermal expansion level; (b) low aggregate thermal expansion level. Error bars represent the standard deviation of the average of three samples.

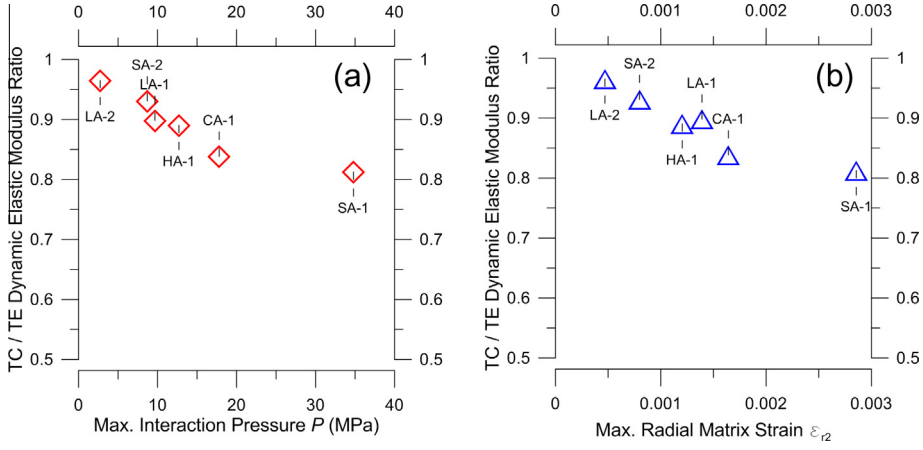

Fig. 13. (a) TC/TE elastic Young's modulus ratios correlated with P values; (b) TC/TE elastic Young's modulus ratios correlated with ε_{r2} values.

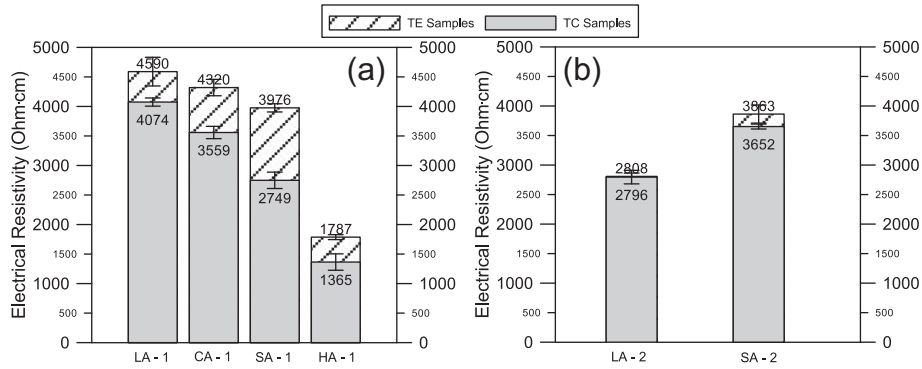

Fig. 14. Electrical resistivity results of TC and TE specimens: (a) high aggregate thermal expansion level; (b) low aggregate thermal expansion level. Error bars represent the standard deviation of the average of three samples.

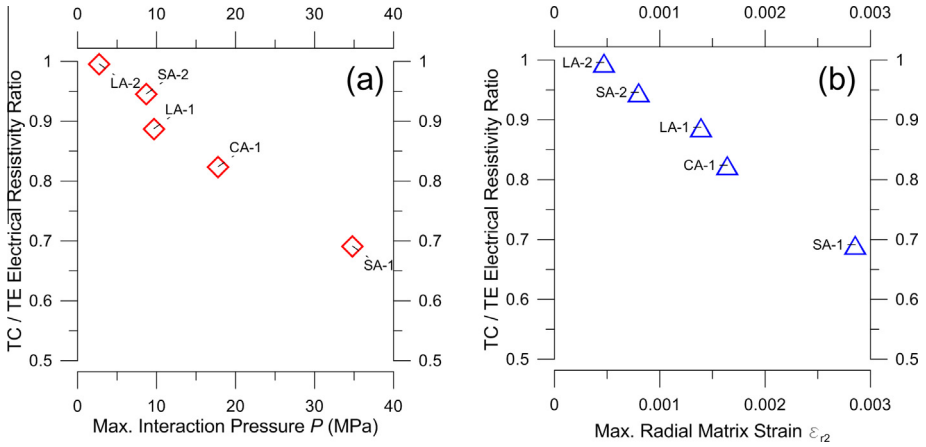

Fig. 15. (a) TC/TE electrical resistivity ratios correlated with P values; (b) TC/TE electrical resistivity ratios correlated with ε_{r2} values.

In this case, a linear trend was observed between the elastic Young's modulus losses represented by the ratios and the maximum P and ε_{r2}.

7.4. Electrical resistivity

The electrical resistivity tests were intended as an indication of concrete percolation due to microcrack propagation. This and other common permeability tests, i.e., the ASTM C1202 rapid chloride penetration test, are based on the assumption that a variation in electrical current passing through the concrete specimen can be attributed to pore and microcrack interconnection and thus to a higher concrete permeability [7,77–79]. For this reason, the inclusion of a conductive material inside the concrete could lead to misleading results because an increase in the current passing through concrete could be attributed not only to increased permeability but also to the presence of the conductive material. The HA aggregates have a high iron content, which is evidenced in its pronounced ferromagnetic behavior, and therefore, the electrical resistivity results do not apply to the HA specimens.

The results of electrical resistivity measurements are presented in Fig. 14 using the same data distribution described for the compressive strength and dynamic elastic Young's modulus. As expected, the electrical resistivity values of the HA-1 specimens are significantly lower than those of other specimens containing non-conductive aggregates. Because the bulk matrix is the same in all concrete specimens considered in this study, the difference is attributed to the conductive characteristics of this particular aggregate type.

As observed from the mechanical properties, the major relative permeability increases are observed in the SA-1 and CA-1 specimens (Fig. 14a). For the low aggregate expansion series (Fig. 14b), no statistically significant difference was observed in LA-2, and a slight increase in permeability was measured in the SA-2 specimens subjected to a time–temperature cycle. Due to the conductive character of the HA aggregate, the results cannot be attributed only to an increased permeability. The aggregate proportion in each particular 10×20 cm cylinder, which might vary due to the compaction procedure [80], could affect the results of this particular specimen group.

For this reason, these results were excluded from the statistical comparison between the electrical resistivity ratios and maximum P and ε_{r2} values; these results are shown on Fig. 15a and b, respectively, and a linear trend was observed between the resistivity losses represented by the ratios and the maximum P and ε_{r2}.

8. Conclusions

Thermal stresses are generated in early-age concrete due to heat release from the ongoing cement hydration. Because concrete is a complex mixture of different constituents, thermo-mechanical mismatches occur, which generate differential expansion between the concrete phases, resulting in stresses. These stresses occur when the cementitious matrix begins to develop stiffness and thus restricts the expansion of the concrete phases. In addition, the matrix tensile strength undergoes early stages of development, leaving the concrete prone to microcracking and damage due to this effect.

The objective of this study was to understand the driving mechanical factors that control the thermal stress generation in the interface between the aggregate and the bulk matrix. A two-phase (aggregates and bulk matrix) micromechanical model was proposed to predict the thermal stresses based on thermo-mechanical mismatches between concrete phases. Two main mismatches were identified: CTE mismatch and elastic mismatch.

Extensive characterization of the concrete phases was carried out to ensure proper modeling of the thermal stresses and thus enable the comparison of these predictions with the observed performance under experimental conditions. These conditions were intended to damage the concrete using time–temperature cycles imposed in a controlled laboratory environment. Based on the experimental measurements and theoretical calculations, the following conclusions can be stated:

1. A simplified two-phase concrete model showed to be useful for prediction of damage to concrete from the thermal stresses. Additionally, the non-complex form of the expressions derived from this model makes it suitable for application to thermal cracking risk assessment in real structures and mixture design procedures based on thermo-mechanical characterization of concrete constituents. Despite it has been shown that the ITZ is the locus of all damage observed, the simplified two-phase model showed to be reliable to estimate the order of magnitude of the impact of thermal cracking on strength, elastic modulus and permeability.
2. The interaction pressure P showed to be a good parameter for estimating the thermal cracking damage expressed as the deterioration in compressive strength, modulus of elasticity, and permeability. To accurately apply the proposed model and compute P, a careful thermo-mechanical characterization (CTE and elastic Young's modulus) of the concrete phases should be carried out.

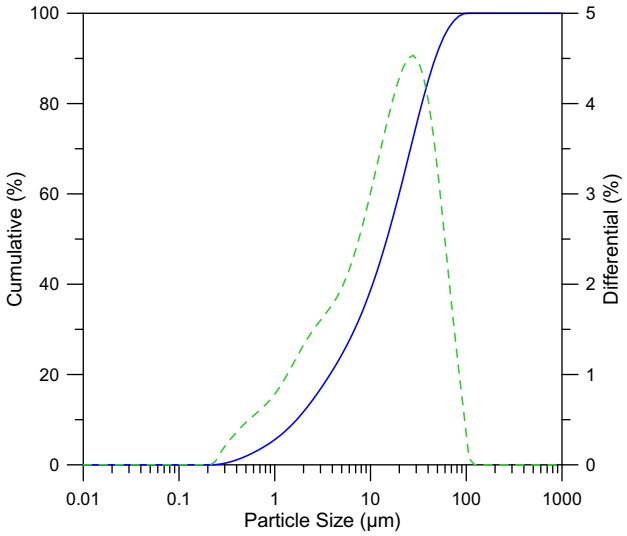

Fig. A.1. OPC particle size distribution (PSD). The solid line represents the cumulative PSD, and the dashed line corresponds to the differential results.

3. Fluorescence microscopy was demonstrated as a valuable tool for evaluating the presence and morphology of damage at the ITZ. This approach is particularly relevant to relate the observed damage with the computed thermal stresses.
4. Considering the high variability in the thermo-mechanical properties of aggregates of natural origin, such as those used in this study, the model is able to produce an order of magnitude of the expected deterioration of the considered concrete properties. Although alternatives to measuring the CTE and stiffness of coarse aggregates were presented in this study, the inherent difficulties in measuring these properties in aggregates of irregular shape poses additional challenges to the development of new testing methods for accurate measurement of these parameters in a more simple and direct manner.

The elastic approach used in this study neglects the time–dependent behavior in cement paste, i.e., creep and stress relaxation, and thus, it tends to overestimate the stresses in the ITZ. However, the strain and interaction pressure P calculations allowed for a good estimate of the thermal damage level. In addition, particle interactions are not considered and thus, the model is only valid at the dilute limit. This simplification may impact on the absolute values of the interaction pressure, but keeps the model in a simpler form requiring only the main thermo-mechanical variables to be computed.

Further research is required to assess the effects of cement substitutions, the use of admixtures, variations in the mixture proportions, and other design properties on the thermo-mechanical parameters. Future work is needed to understand and develop new methodologies that reduce the thermal cracking risk at the design stage and to address the thermo-mechanical compatibility orientation, rather than mitigating heat release at the construction site.

Acknowledgements

The authors greatly acknowledge funding provided by FONDECYT – Chile, project N°1120817 and the support provided by CEDEUS, CONICYT/FONDAP – Chile 15110020. The authors also recognize Cementos Polpaico, CAP Minería, DICTUC S.A., Sebastián Calderón and Mauricio Guerra for their contributions to this research project.

Appendix A. OPC physical and chemical characterization

The Type I OPC chemical composition presented in terms of oxides measured with X-ray fluorescence (XRF) is shown in Table A.1, and the particle size distribution (PSD) is presented in Fig. A.1.

The X-Ray diffraction pattern of the employed OPC is shown on Fig. A.2.

Table A.1
Cement chemical characterization.

Composition as oxides (%)	OPC
SiO_2	20.39
Al_2O_3	6.01
Fe_2O_3	3.15
CaO	63.25
Na_2O	0.15
K_2O	0.75
MnO	0.07
TiO_2	0.27
MgO	1.30
P_2O_5	0.08
SrO	0.03
SO_3	2.35
LOI	1.72
Specific gravity (g/cm^3)	3.122

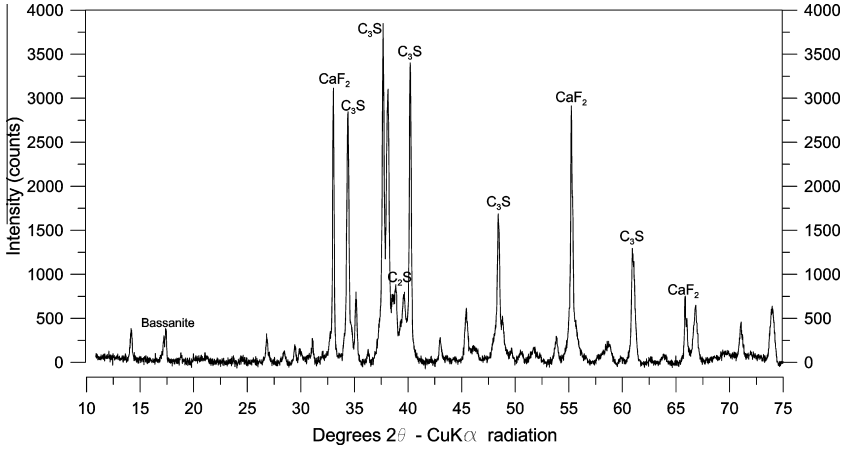

Fig. A.2. X-ray diffraction pattern of the OPC used for the Rietveld refinement.

References

[1] Mehta P, Monteiro P. Concrete: microstructure, properties, and materials. 3rd ed. New York: McGraw-Hill Professional; 2005.
[2] Bentz DP, Jensen OM. Mitigation strategies for autogenous shrinkage cracking. Cem Concr Compos 2004;26:677–85. http://dx.doi.org/10.1016/S0958-9465(03)00045-3.
[3] Mehta P. Durability – critical issues for the future. Concr Int 1997;19:69–76.
[4] Jensen OM, Hansen PF. Autogenous deformation and RH-change in perspective. Cem Concr Res 2001;31:1859–65.
[5] Holt E. Contribution of mixture design to chemical and autogenous shrinkage of concrete at early ages. Cem Concr Res 2005;35:464–72. http://dx.doi.org/10.1016/j.cemconres.2004.05.009.
[6] Gowripalan N, Sirivivatnanon V, Lim CC. Chloride diffusivity of concrete cracked in flexure. Cem Concr Res 2000;30:725–30. http://dx.doi.org/10.1016/S0008-8846(00)00216-7.
[7] Konin A, François R, Arliguie G. Penetration of chlorides in relation to the microcracking state into reinforced ordinary and high strength concrete. Mater Struct 1998;31:310–6.
[8] Samaha HR, Hover KC. Influence of microcracking on the mass transport properties of concrete. ACI Mater J 1992;89:416–24.
[9] Wang K, Jansen DC, Shah SP, Karr AF. Permeability study of cracked concrete. Cem Concr Res 1997;27:381–93.
[10] ACI 231R. Report on early-age cracking: causes, measurement, and mitigation; 2010.
[11] Schindler AK. Effect of temperature on hydration of cementitious materials. ACI Mater J 2004;101:72–81.
[12] Gallucci E, Zhang X, Scrivener KL. Effect of temperature on the microstructure of calcium silicate hydrate (C–S–H). Cem Concr Res 2013;53:185–95. http://dx.doi.org/10.1016/j.cemconres.2013.06.008.
[13] Escadeillas G, Aubert J-E, Segerer M, Prince W. Some factors affecting delayed ettringite formation in heat-cured mortars. Cem Concr Res 2007;37:1445–52. http://dx.doi.org/10.1016/j.cemconres.2007.07.004.
[14] Taylor H, Famy C, Scrivener K. Delayed ettringite formation. Cem Concr Res 2001;31:683–93. http://dx.doi.org/10.1016/S0008-8846(01)00466-5.
[15] Zhang Z, Olek J, Diamond S. Studies on delayed ettringite formation in early-age, heat-cured mortars I. Expansion measurements, changes in dynamic modulus of elasticity, and weight gains. Cem Concr Res 2002;32:1729–36.
[16] ACI 207-2R. Report on thermal and volume change effects on cracking of mass concrete; 2007.
[17] ACI 224.1R. Causes, evaluation, and repair of cracks in concrete structures; 2007.
[18] Alexander MG. Aggregates and the deformation properties of concrete. ACI Mater J 1997;93.
[19] Bremner TW, Holm TA. Elastic compatibility and the behavior of concrete. ACI J 1986;83:244–50.
[20] Selsing J. Internal stresses in ceramics. J Am Ceram Soc 1961;44:419.
[21] Zhou C, Huang B, Ph D, Asce M, Shu X, Asce AM. Micromechanical model for predicting coefficient of thermal expansion of concrete. J Mater Civ Eng 2013;25:1171–80. http://dx.doi.org/10.1061/(ASCE)MT.1943-5533.0000663.
[22] Lee KM, Park JH. A numerical model for elastic modulus of concrete considering interfacial transition zone. Cem Concr Res 2008;38:396–402. http://dx.doi.org/10.1016/j.cemconres.2007.09.019.
[23] Nilsen AU, Monteiro PJM. Concrete: a three phase material. Cem Concr Res 1993;23:147–51.
[24] Scrivener, Crumbie A, Laugesen P. The interfacial transition zone (ITZ) between cement paste and aggregate. Interface Sci 2004;12:411–21.
[25] Noumowe AN, Siddique R, Debicki G. Permeability of high-performance concrete subjected to elevated temperature (600 °C). Constr Build Mater 2009;23:1855–61. http://dx.doi.org/10.1016/j.conbuildmat.2008.09.023.
[26] Lee Y, Choi M-S, Yi S-T, Kim J-K. Experimental study on the convective heat transfer coefficient of early-age concrete. Cem Concr Compos 2009;31:60–71. http://dx.doi.org/10.1016/j.cemconcomp.2008.09.009.
[27] Qian C, Gao G. Reduction of interior temperature of mass concrete using suspension of phase change materials as cooling fluid. Constr Build Mater 2012;26:527–31. http://dx.doi.org/10.1016/j.conbuildmat.2011.06.053.
[28] Lin F, Song X, Gu X, Peng B, Yang L. Cracking analysis of massive concrete walls with cracking control techniques. Constr Build Mater 2012;31:12–21. http://dx.doi.org/10.1016/j.conbuildmat.2011.12.086.
[29] Wei Y, Hansen W. Early-age strain–stress relationship and cracking behavior of slag cement mixtures subject to constant uniaxial restraint. Constr Build Mater 2013;49:635–42. http://dx.doi.org/10.1016/j.conbuildmat.2013.08.061.
[30] Pourasee A, Peled A, Weiss J, Asce M. Fluid transport in cracked fabric-reinforced-cement-based composites. ASCE J Mater Civ Eng 2011:1227–38. http://dx.doi.org/10.1061/(ASCE)MT.1943-5533.0000289.
[31] Yang Z, Weiss WJ, Olek J. Water transport in concrete damaged by tensile loading and freeze – thaw cycling. ASCE J Mater Civ Eng 2006:424–34.
[32] Bentz DP, Garboczi EJ, Lu Y, Martys N, Sakulich AR, Weiss WJ. Modeling of the influence of transverse cracking on chloride penetration into concrete. Cem Concr Compos 2013;38:65–74. http://dx.doi.org/10.1016/j.cemconcomp.2013.03.003.
[33] Zhu W, Bartos PJ. Application of depth-sensing microindentation testing to study of interfacial transition zone in reinforced concrete. Cem Concr Res 2000;30:1299–304. http://dx.doi.org/10.1016/S0008-8846(00)00322-7.
[34] Xiao J, Li W, Sun Z, Lange Da, Shah SP. Properties of interfacial transition zones in recycled aggregate concrete tested by nanoindentation. Cem Concr Compos 2013;37:276–92. http://dx.doi.org/10.1016/j.cemconcomp.2013.01.006.
[35] Erdem S, Dawson AR, Thom NH. Influence of the micro- and nanoscale local mechanical properties of the interfacial transition zone on impact behavior of concrete made with different aggregates. Cem Concr Res 2012;42:447–58. http://dx.doi.org/10.1016/j.cemconres.2011.11.015.
[36] Trtik P, Bartos PJM. Micromechanical properties of cementitious composites. Mater Struct 1999;32:388–93.
[37] Zhu W, Bartos PJ. Assessment of interfacial microstructure and bond properties in aged grc using a novel microindentation method. Cem Concr Res 1997;27:1701–11.
[38] Wang XH, Jacobsen S, He JY, Zhang ZL, Lee SF, Lein HL. Application of nanoindentation testing to study of the interfacial transition zone in steel fiber reinforced mortar. Cem Concr Res 2009;39:701–15. http://dx.doi.org/10.1016/j.cemconres.2009.05.002.
[39] Hirsch TJ. Modulus of elasticity of concrete affected by elastic moduli of cement paste matrix and aggregate. ACI J 1962;59:427–52.
[40] Chen H, Yen T, Chen K. Evaluating elastic modulus of lightweight aggregate. ACI Mater J 2003;100:108–13.
[41] Nilsen AU, Monteiro PJM, Gjcrv OE. Estimation of the elastic moduli of lightweight aggregate. Cem Concr Res 1995;25:276–80.
[42] Neville A. Properties of concrete. 4th ed. Essex: Pearson Education Limited; 1995.
[43] Lopez M, Kahn LF, Kurtis KE. Characterization of elastic and time-dependent deformations in normal strength and high performance concrete by image analysis. Cem Concr Res 2007;37:1265–77. http://dx.doi.org/10.1016/j.cemconres.2007.05.011.
[44] ACI 209.1R. Report on factors affecting shrinkage and creep of hardened concrete; 2005.
[45] Jeong J, Ramézani H, Leklou N. Thermo-chemical heterogeneous hydration gradient modeling of concrete and aggregates size effect on ITZ. Thermochim Acta 2014;590:165–80. http://dx.doi.org/10.1016/j.tca.2014.06.019.
[46] Burgreen D. Elements of thermal stress analysis. London: Arcturus Publishing; 1971.
[47] Akçaoğlu T, Tokyay M, Çelik T. Effect of coarse aggregate size and matrix quality on ITZ and failure behavior of concrete under uniaxial compression. Cem Concr Compos 2004;26:633–8. http://dx.doi.org/10.1016/S0958-9465(03)00092-1.
[48] Tank RC, Carino NJ. Rate constant functions for strength development of concrete. ACI Mater J 1991;88:74–83.
[49] Abdel-Jawad YA. The maturity method: modifications to improve estimation of concrete strength at later ages. Constr Build Mater 2006;20:893–900. http://dx.doi.org/10.1016/j.conbuildmat.2005.06.022.
[50] Saul AGA. Principles underlying the steam curing of concrete at atmospheric pressure. Mag Concr Res 1951;2:127–40.
[51] Chengju G. Maturity of concrete: method for predicting early- stage strength. ACI Mater J 1989:341–53.
[52] Deschutter G. Applicability of degree of hydration concept and maturity method for thermo-visco-elastic behaviour of early age concrete. Cem Concr Compos 2004;26:437–43. http://dx.doi.org/10.1016/s0958-9465(03)00067-2.
[53] ASTM C1074. Standard practice for estimating concrete strength by the maturity method; 2004. http://dx.doi.org/10.1520/C1074-04.2.
[54] Yi S-T, Moon Y-H, Kim J-K. Long-term strength prediction of concrete with curing temperature. Cem Concr Res 2005;35:1961–9. http://dx.doi.org/10.1016/j.cemconres.2005.06.010.
[55] Poole JL, Asce M, Riding KA, Juenger MCG, Folliard KJ, Schindler AK. Effect of chemical admixtures on apparent activation energy of cementitious systems. ASCE J Mater Civil Eng 2011;23:1654–61. http://dx.doi.org/10.1061/(ASCE)MT.1943-5533.0000345.
[56] Zhang M, Tam C, Leow M. Effect of water-to-cementitious materials ratio and silica fume on the autogenous shrinkage of concrete. Cem Concr Res 2003;33:1687–94. http://dx.doi.org/10.1016/S0008-8846(03)00149-2.
[57] Barcelo L, Moranville M, Clavaud B. Autogenous shrinkage of concrete: a balance between autogenous swelling and self-desiccation. Cem Concr Res 2005;35:177–83. http://dx.doi.org/10.1016/j.cemconres.2004.05.050.
[58] Pichler C, Lackner R, Mang Ha. A multiscale micromechanics model for the autogenous-shrinkage deformation of early-age cement-based materials. Eng Fract Mech 2007;74:34–58. http://dx.doi.org/10.1016/j.engfracmech.2006.01.034.
[59] Pane L, Hansen W. Early age creep and stress relaxation of concrete containing blended cements. Mater Struct 2002;35:92–6.
[60] Bentz DP. A review of early-age properties of cement-based materials. Cem Concr Res 2008;38:196–204. http://dx.doi.org/10.1016/j.cemconres.2007.09.005.
[61] Litorowicz A. Identification and quantification of cracks in concrete by optical fluorescent microscopy. Cem Concr Res 2006;36:1508–15. http://dx.doi.org/10.1016/j.cemconres.2006.05.011.
[62] Soroushian P, Elzafraney M, Nossoni A. Specimen preparation and image processing and analysis techniques for automated quantification of concrete microcracks and voids. Cem Concr Res 2003;33:1949–62. http://dx.doi.org/10.1016/S0008-8846(03)00219-9.
[63] Jakobsen UH, Brown DR. Reproducibility of w/c ratio determination from fluorescent impregnated thin sections. Cem Concr Res 2006;36:1567–73. http://dx.doi.org/10.1016/j.cemconres.2006.05.003.

[64] Soroushian P, Elzafraney M. Morphological operations, planar mathematical formulations, and stereological interpretations for automated image analysis of concrete microstructure. Cem Concr Compos 2005;27:823–33. http://dx.doi.org/10.1016/j.cemconcomp.2004.07.008.
[65] ASTM C215. Standard test method for fundamental transverse, longitudinal, and torsional resonant frequencies of concrete specimens; 2008. http://dx.doi.org/10.1520/C0215-08.2.
[66] Spragg RP, Castro J, Nantung T, Paredes M, Weiss J. Variability analysis of the bulk resistivity measured using concrete cylinders. Adv Civil Eng Mater 2012;1:1–17. http://dx.doi.org/10.1520/ACEM104596.
[67] Morris W, Moreno EI, Sagüés AA. Practical evaluation of resistivity of concrete in test cylinders using a Wenner array probe. Cem Concr Res 1996;26:1779–87.
[68] Siddiqui S, Riding KA. Effect of calculation methods on cement paste and mortar apparent activation energy. Adv Civil Eng Mater 2012;1:1–19. http://dx.doi.org/10.1520/ACEM20120011.
[69] Poole JL, Riding KA, Folliard KJ, Juenger MCG, Schindler AK. Methods for calculating activation energy for Portland cement. ACI Mater J 2007;104:303–11.
[70] Chancey RT, Stutzman P, Juenger MCG, Fowler DW. Comprehensive phase characterization of crystalline and amorphous phases of a Class F fly ash. Cem Concr Res 2010;40:146–56. http://dx.doi.org/10.1016/j.cemconres.2009.08.029.
[71] Bogue RH. The chemistry of Portland cement. New York: Reinhold; 1947.
[72] Maruyama I, Teramoto A. Effect of water-retaining lightweight aggregate on the reduction of thermal expansion coefficient in mortar subject to temperature histories. Cem Concr Compos 2012;34:1124–9. http://dx.doi.org/10.1016/j.cemconcomp.2012.08.003.
[73] Jiang Z, Sun Z, Wang P. Autogenous relative humidity change and autogenous shrinkage of high-performance cement pastes. Cem Concr Res 2005;35:1539–45. http://dx.doi.org/10.1016/j.cemconres.2004.06.028.
[74] Baroghel-Bouny V, Mounanga P, Khelidj A, Loukili A, Rafaï N. Autogenous deformations of cement pastes. Cem Concr Res 2006;36:123–36. http://dx.doi.org/10.1016/j.cemconres.2004.10.020.
[75] Moreno D, Martinez P, Lopez M. Practical approach for assessing lightweight aggregate potential for concrete performance. ACI Mater J 2014;111:123–32.
[76] Lim C, Gowripalan N, Sirivivatnanon V. Microcracking and chloride permeability of concrete under uniaxial compression. Cem Concr Compos 2000;22:353–60. http://dx.doi.org/10.1016/S0958-9465(00)00029-9.
[77] Riding KA, Poole JL, Schindler AK, Juenger MCG, Folliard KJ. Simplified concrete resistivity and rapid chloride permeability test method 2009:1–5.
[78] Corral R, Arredondo S, Almaral J, Gómez J. Corrosión por cloruros del acero de refuerzo embebido en concreto con agregado grueso reciclado y materiales cementantes suplementarios. Rev Ing Constr 2013;28:21–35. http://dx.doi.org/10.4067/SO718-50732013000100002.
[79] Saraswathy V, Song H-W. Corrosion performance of rice husk ash blended concrete. Constr Build Mater 2007;21:1779–84. <http://www.sciencedirect.com/science/article/B6V2G-4M3RP2B-1/2/49beade1a621425192f05488974460e3>.
[80] Moreno D, Zunino F, Paul Á, Lopez M. High strength lightweight concrete (HSLC): challenges when moving from the laboratory to the field. Constr Build Mater 2014;56:44–52. http://dx.doi.org/10.1016/j.conbuildmat.2014.01.068.